



# A theoretical and experimental investigation of continuous oil–water gravity separation

Moein Assar<sup>a</sup>, Hamidreza Asaadian<sup>b</sup>, Milan Stanko<sup>b</sup>, Brian Arthur Grimes<sup>a,\*</sup>

<sup>a</sup> Ugelstad Laboratory, Department of Chemical Engineering, Norwegian University of Science and Technology (NTNU), N-7491 Trondheim, Norway

<sup>b</sup> Petroleumsteknisk senter, Norwegian University of Science and Technology (NTNU), N-7491 Trondheim, Norway

## ARTICLE INFO

### Keywords:

Population balance model  
Multiphase fluid  
Particulate system  
Gravity separation  
Emulsion  
Separator

## ABSTRACT

In this study, we have developed a mathematical model for a three-phase separator. The model consists of two sections: the inlet section and the separation section, separated by a perforated calming baffle. In the inlet section, two dispersion layers undergo droplet size evolution due to turbulent breakage and coalescence, described by a spatially homogeneous PBE. In the separation section, the two dispersion layers flow alongside each other and interact at an interface. The volumetric flow and velocity profiles are influenced by interfacial coalescence, with considerations for plug and laminar flow assumptions. The model incorporates droplet gravity-driven transport using the Kumar and Hartland model, binary and interfacial coalescence employing a film drainage model, and an effective diffusion term to account for the formation of the dense packed layer which ensures a physical volume fraction range of 0–1. Steady-state and transient numerical solvers are developed to solve the resulting advection–diffusion equations. Additionally, a series of experiments were conducted using a lab-scale multi-parallel pipes separator to investigate the impact of varying volume fractions and flow rates on the separation efficiency of the equipment. The model results are compared with the experimental data which shows relatively good agreement.

## 1. Introduction

Gravitational separators play a vital role in the crude oil industry due to their cost-effectiveness and simplicity (Panjwani et al., 2015). The significance of this process has been further amplified by the escalating production of water in existing oil fields and the extraction of heavier crude oil reserves. The behavior and stability of emulsions encountered in the petroleum industry can vary extensively, mainly due to the compositional variations in crude oil and water (Oshinowo et al., 2016). The aforementioned challenge has posed significant difficulties in developing an inclusive model for oil/water separation. Building such a model has proven to be a complex task due to the multitude of assumptions and varying levels of complexity involved.

In their study, Wang and Davis (1995) investigated a batch separation process that involved concurrent sedimentation and coalescence of droplets. They employed simplifications in their modeling approach, such as assuming a dilute dispersion and neglecting resistance to interfacial coalescence. Cunha et al. (2008) devised their PBE model for simultaneous sedimentation and Brownian motion, considering Stokes terminal velocity and binary droplet coalescence. They made several

assumptions, including a proportional interfacial coalescence velocity with the height of the dense packed layer (DPL). Additionally, they introduced three tuning parameters for the droplet terminal velocity, binary coalescence rate, and interfacial coalescence rate to align the model with their experimental observations of a crude oil–water system. Grimes (2012) developed a model by incorporating the hindered settling velocity model initially proposed by Richardson and Zaki (1955), along with a film drainage model to account for simultaneous binary and interfacial coalescence. To handle the complex issue of the moving boundary arising from homophase growth, Grimes employed a temporal-spatial transformation approach. In a subsequent publication (Grimes et al., 2012), the model's validity and accuracy were demonstrated through comparisons with experimental data.

Antonio García and Fernando Betancourt (2019) proposed their model by adopting various coalescence rates. They utilized the coalescence model of Rogers and Davis (1990) for the sedimentation zone while coalescence rate by Ruiz and Padilla (1996) was utilized for the DPL. The droplet slip velocity was estimated using the Kumar and Hartland equation (Kumar and Hartland, 1985). Their model also incorporated a correction procedure to deactivate the coalescence birth

\* Corresponding author.

E-mail address: [brian.a.grimes@ntnu.no](mailto:brian.a.grimes@ntnu.no) (B.A. Grimes).

<https://doi.org/10.1016/j.ces.2024.120375>

Received 18 February 2024; Received in revised form 5 June 2024; Accepted 11 June 2024

Available online 15 June 2024

0009-2509/© 2024 The Author(s). Published by Elsevier Ltd. This is an open access article under the CC BY license (<http://creativecommons.org/licenses/by/4.0/>).

term for unphysical volume fraction values exceeding unity. In a subsequent study, they expanded the model to simulate continuous separators (Antonio García et al., 2022). Assar et al. (2023) made another progress in this field by presenting a mathematical model for batch separation processes. They conducted a comparative analysis of various models for droplet slip velocity and concluded that the Kumar and Hartland model yields better agreement with experimental data. Another important aspect of their work involves mathematical model for the formation of the DPL. To address this, they introduced effective diffusion into the model as an advection–diffusion equation. They selected a suitable closure model for the effective diffusion coefficient to ensure the physical volume fraction range (0–1). Finally, they fine-tuned the proposed closure model using experimental data obtained from NMR (Nuclear Magnetic Resonance) techniques with a wide range of water volume fractions (20–60 %).

An alternative approach in modeling involves the combination of the population balance equation and computational fluid dynamics (PBE-CFD) using readily available CFD software packages. Panjwani et al. (2015) employed such a model to investigate the DPL in a continuous separator. Oshinowo et al. (2016) applied a multi-fluid Eulerian multi-phase approach to model batch separation and validated their model against experimental data obtained through the ultrasonic technique. In a subsequent study (Oshinowo and Vilagines, 2020), they applied a similar model to a three-phase separator.

The CFD-PBE approach encounters certain challenges due to its computational complexity and resource-intensive nature. These factors can pose limitations on its practical application in various engineering scenarios, including design, model tuning, facilitating scale-ups, process control, and process optimization. Moreover, incorporating the internal components of a three-phase separator, such as the inlet device or calming baffle, into these CFD models presents difficulties and restrictions that are often overlooked in related studies. However, the majority of industrial three-phase separators operate with these internal elements, which their presence significantly impacts the overall efficiency of the process.

Accordingly, the development of an effective model for oil/water separation faces several challenges that need to be addressed. These challenges include considering dispersion in both aqueous and hydrocarbon phases, accurately defining the interfacial coalescence between the layers, accounting for hydrodynamic effects, addressing inlet device and turbulence-induced breakage at the inlet section of a separator, and ensuring computational efficiency and robustness for widespread use in various engineering activities. In this paper, we have made efforts to tackle these challenges by striking a balance between the complexity of the physical phenomena included in the model and computational efficiency. The proposed model aims to capture the underlying physical mechanisms in the system to a significant extent, while still incorporating some tuning parameters to compensate for simplifying assumptions. This approach allows for a more comprehensive understanding of the system while maintaining practical usability and computational feasibility.

Furthermore, a series of experiments were conducted utilizing a lab-scale multi-parallel pipes separator to investigate the influence of varying volume fractions and flow rates on the equipment's separation efficiency. Subsequently, the model predictions are validated against the experimental findings.

## 2. Mathematical model

The three-phase separator is divided into two sections: the inlet section and the separation section, as depicted in Fig. 1a. These sections are separated by a perforated thick plate usually known as a calming baffle. In the inlet section, the flow is typically turbulent and chaotic. The purpose of the calming baffle is to smoothen the flow, allowing droplets to coalesce and settle under the influence of the gravity.

The model proposed in this study is distinctive in its incorporation of both dispersion and creaming in oil-in-water and dispersion and sedimentation in water-in-oil emulsions, ensuring its generality. Nevertheless, for the purpose of comparing with experimental data, the model exclusively considers creaming in oil-in-water emulsion.

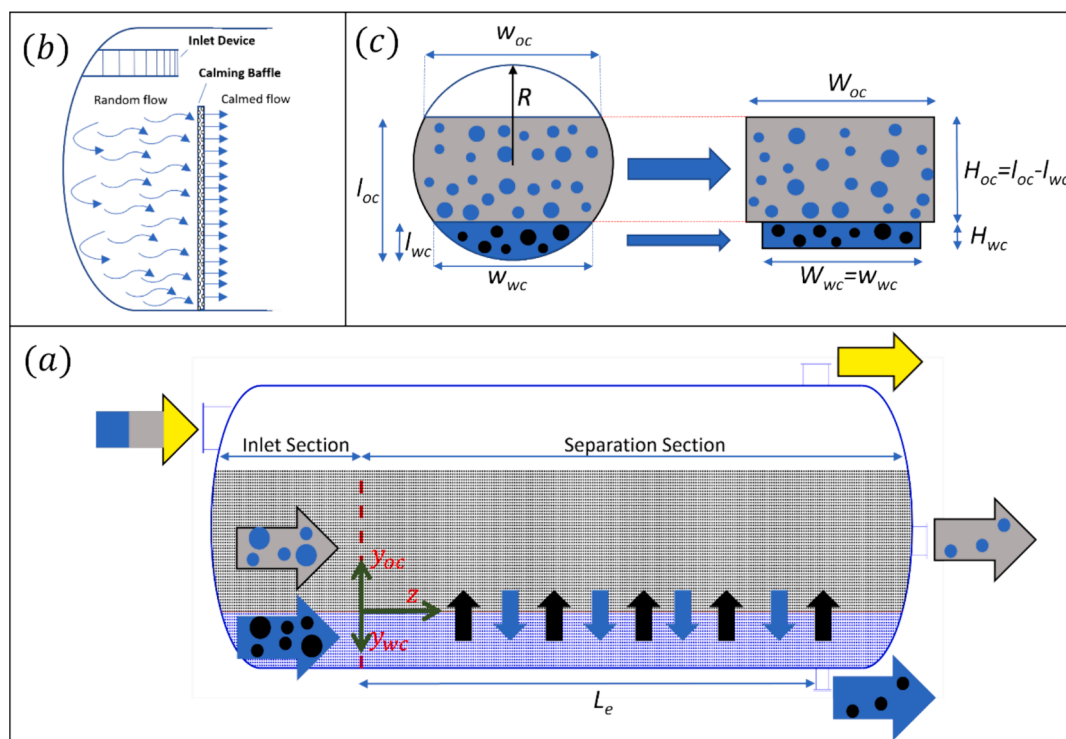


**Fig. 1.** (a) Schematic of a three-phase separator with oil-continuous, water-continuous and vapor phases, inlet and separation sections are separated using a calming baffle. (b) Inlet section encompassing an inlet device (c) geometrical averaging and transforming the circular segments to rectangles.

The sub-models for the two sections are as follows.

### 2.1. Inlet section model

Fig. 1b illustrates the schematic representation of the inlet section in a separator. The three-phase flow is delivered into this section through the inlet device. The assumption is made that the gas phase separates completely from the liquid phase. Furthermore, it is assumed that the liquid phase partially separates into two dispersions: oil-in-water (wc: water-continuous) and water-in-oil (oc: oil-continuous). These dispersions then undergo droplet size evolution as a result of turbulence-induced breakage and coalescence processes.

#### 2.1.1. Partial water–oil separation

Backi et al. (2018) introduced the concept of split factors to describe the partial separation of water and oil in the inlet section. These split factors, denoted as  $\varphi_o$  and  $\varphi_w$ , are used to determine the flow rate and volume fraction of the oil-continuous and water-continuous layers.  $\varphi_o$  and  $\varphi_w$  are equal the volume fraction of the total oil in the oil-continuous layer and fraction of total water in the water-continuous layer, respectively. Typical values suggested by Becki et al. for these split factors ranges between 0.7 and 0.9. The specific values of the split factors are not fixed and can vary depending on the inlet flow rate and flow regime as well as the inlet device type and design. However, these values are still constrained by the inversion point and the ability of fluids to form stable emulsions. Using these split factors, we can calculate the volumetric flow rates ( $Q_{oc}$ ,  $Q_{wc}$ ) and the volume fractions of the dispersed phase ( $\phi_{oc}$ ,  $\phi_{wc}$ ) in oil- and water-continuous dispersion layers as follows:

$$Q_{oc}(t) = \varphi_o Q_o(t) + (1 - \varphi_w) Q_w(t) \quad (1)$$

$$Q_{wc}(t) = \varphi_w Q_w(t) + (1 - \varphi_o) Q_o(t) \quad (2)$$

$$\phi_{oc}(t) = \frac{(1 - \varphi_w)\alpha(t)}{\varphi_o(1 - \alpha(t)) + (1 - \varphi_w)\alpha(t)} \quad (3)$$

$$\phi_{wc}(t) = \frac{(1 - \varphi_o)(1 - \alpha(t))}{\varphi_w\alpha(t) + (1 - \varphi_o)(1 - \alpha(t))} \quad (4)$$

where  $Q_o$  and  $Q_w$  are total oil and water volumetric flows, and  $\alpha$  is the water cut in the inlet liquid stream. Alternatively, if the volume fractions of the dispersed layers are known, the volumetric flow rates can be calculated using the following equations:

$$Q_{oc}(t) = \frac{Q_o(t) - \phi_{wc}(Q_o(t) + Q_w(t))}{1 - \phi_{oc} - \phi_{wc}} \quad (5)$$

$$Q_{wc}(t) = \frac{Q_w(t) - \phi_{oc}(Q_o(t) + Q_w(t))}{1 - \phi_{oc} - \phi_{wc}} \quad (6)$$

#### 2.1.2. Dispersion model

The dispersions arriving to the inlet section partially split and go through droplet size evolution due to turbulence-induced breakage and coalescence mechanisms. The evolution of droplets size in each dispersion layer can be expressed by a population balance equation (PBE) for a spatially homogeneous chamber with inflow and outflow as below:

$$\begin{aligned} \frac{\partial f_{IS,i}(r_i, t)}{\partial t} = & \int_{r_i}^{\infty} 2\gamma_{t,i}(r_i', t)\beta(r_i', r_i)f_{IS,i}(r_i', t)\frac{r_i'^3}{r_i^3}dr_i' \\ & - \gamma_{t,i}(r_i, t)f_{IS,i}(r_i, t) + \left(\frac{3}{4\pi}\right) \times \\ & \int_0^{\frac{r_i}{\sqrt{2}}} \kappa_{t,i}(r_i', r_i'', t)f_{IS,i}(r_i', t)f_{IS,i}(r_i'', t)\frac{r_i'^5}{r_i^3 r_i''^5}dr_i' \\ & - \left(\frac{3}{4\pi}\right)f_{IS,i}(r_i, t) \int_0^{\infty} \kappa_{t,i}(r_i', r_i, t)f_{IS,i}(r_i', t)\frac{dr_i'}{r_i^3} \\ & + \frac{1}{t_{r,IS}(t)} [f_{in,i}(r_i, t) - f_{IS,i}(r_i, t)] \quad \forall r_i | 0 \leq r_i \leq \infty, \quad t | 0 < t \leq t_f \end{aligned} \quad (7)$$

where the subscript  $i$  shows the dispersion layer (oc: oil-continuous and wc: water-continuous).  $f_{IS,i}(r_i, t)$  is the radius-based volume density distribution of droplet size  $r_i$  in the inlet section (refer to Assar et al. (2023) for derivation of radius-based PBE);  $r_i$  is the droplet radius;  $t$  is time;  $t_{r,IS}(t)$  is the average residence time in the inlet chamber and is calculated as the liquid volume of the inlet section divided by the total flow rate of oil and water. Importantly, the time functionality in this term will allow to capture transient variations in the liquid level.  $\gamma_{IS,i}(r_i, t)$  is the breakage frequency of droplet size  $r_i$ ;  $\beta(r_i', r_i)$  is radius-based daughter distribution of droplet radius  $r_i$  resultant from binary breakage of droplet size  $r_i'$ ;  $\kappa_{IS,i}(r_i', r_i, t)$  is the coalescence rate between droplet sizes of  $r_i'$  and  $r_i$ ,  $r_i''$  in the coalescence birth rate term is equal to  $(r_i^3 - r_i'^3)^{1/3}$ .  $f_{in,i}$  represents the droplet size distribution of the inlet flow. This inlet distribution can be affected by the flow regime in the upstream pipeline. Additionally, presence of processes generating high shear rates such as pump and choke valves can significantly reduce the inlet droplet size distribution received at the separator. Eq. (7) can be solved subject to the below initial condition:

$$f_{IS,i}(r_i, t) = f_{IS,i,0}(r_i) \text{ at } t = 0, \quad \forall r_i | 0 \leq r_i \leq \infty \quad (8)$$

In the turbulent and chaotic flow of the inlet section, the predominant phenomena are droplet breakage and binary coalescence caused by turbulent fluctuations. Various kernels have been proposed to model these breakage and coalescence processes. A good summary of that can be found in Bin Ismail (2021). The coalescence rate is normally expressed as the product of collision rate and coalescence efficiency as follows:

$$\kappa_{t,i}(r_i', r_i, t) = \omega_{t,i}(r_i', r_i, t)\psi_{t,i}(r_i', r_i, t) \quad (9)$$

The collision rate function can be selected according to Prince and Blanch (1990) as below:

$$\omega_{t,i}(r_i', r_i, t) = k_{c1}\pi 2 \left(\frac{1}{3}\right) \varepsilon_i(t) \left(\frac{1}{3}\right) (r_i' + r_i)^2 (r_i'^{2/3} + r_i^{2/3}) \left(\frac{1}{2}\right) \quad (10)$$

The coalescence efficiency function can be selected according to Chesters (1991) which is based on the film drainage mechanism between colliding droplets. This function is as follows:

$$\psi_{t,i}(r_i', r_i, t) = \exp \left( -\frac{1}{k_{c2}} 2 \left(-\frac{1}{6}\right) \rho_c \left(\frac{1}{2}\right) \varepsilon_i(t) \left(\frac{1}{3}\right) \left(\frac{1}{r_i'} + \frac{1}{r_i}\right) \left(-\frac{5}{6}\right) \right) \quad (11)$$

The model proposed by Vankova et al. (2007) is employed for the breakage frequency as follows:

$$\gamma_{t,i}(r_i, t) = k_{b1} \frac{\varepsilon_i(t)^{\left(\frac{1}{3}\right)} \left(\frac{\rho_d}{\rho_c}\right)^{\left(\frac{1}{2}\right)} \frac{1}{r_i^{\left(\frac{2}{3}\right)}} \times \exp\left(-\frac{1}{k_{b2}} \frac{\sigma}{2 \rho_{d,i} \varepsilon_i(t)^{\left(\frac{2}{3}\right)} r_i^{\left(\frac{5}{3}\right)}}\right) \quad (12)$$

The daughter size distribution for binary breakage of droplets, by Coualoulou and Tavlarides (1977), is also employed as follows:

$$\beta(r'_i, r_i) = 7.2 \frac{r_i^2}{r_i'^3} \exp\left(-4.5 \frac{(2r_i^3 - r_i'^3)^2}{r_i'^6}\right) \quad (13)$$

The turbulence dissipation rate is the most important parameter for calculating the coalescence and breakage rates. In our model, the inlet section is assumed to be spatially homogeneous. Therefore, in order to solve the equations, the dissipation rate needs to be spatially averaged over the inlet section volume to make it independent of spatial variations. This term can be calculated by considering the kinetic energy of the liquid mixture in the inlet pipe as the main source for generating turbulence in the system. By this assumption, the spatially-averaged turbulence dissipation rate becomes:

$$\varepsilon_i(t) = \frac{\dot{m}_l(t) u_{in}(t)^2 / 2}{\rho_c V_{IS}(t)} \quad (14)$$

The term on the nominator of Eq. (14) is the kinetic energy of the liquid mixture in the inlet pipe to the separator,  $\rho_c$  is the continuous phase density in the dispersion  $i$ , and  $V_{IS}$  is the volume of the inlet section. Eq. (14) can be simplified and rearranged to the following form:

$$\varepsilon_i(t) = \frac{u_{in}(t)^2}{2 t_{r,IS}(t)} \quad (15)$$

The inlet device plays a crucial role in receiving the inlet stream and controlling its momentum to facilitate gas–liquid separation while avoiding undesirable phenomena like foam, tight emulsions, and droplet carryover in vapor phase. For further study on inlet devices, Bothamley (2013) provides a comprehensive analysis. The spatial homogeneity assumption can be compromised by the choice of inlet device types such as diverter plates, reverse pipes, half pipes, and dished heads, which can generate non-uniform flow patterns. However, more advanced designs like vane-type and cyclonic-type inlet devices produce less turbulent local regions in the inlet section.

To thoroughly assess the impact of inlet devices, it is imperative to incorporate the momentum equation, accounting for the inertial and centrifugal forces inherent in these devices. Given the intricate nature of such devices, a 3D analysis becomes essential to capture the entirety of these effects. However, it is noteworthy that this study omits such considerations. Instead, to mitigate uncertainties stemming from the described averaging strategy, the tuning parameters  $k_{c1}$ ,  $k_{c2}$ ,  $k_{b1}$  and  $k_{b2}$  are introduced in Eqs. (10)–(12). These parameters are anticipated to be correlated with the specific type of inlet device as well as inlet flow rates.

Eq. (7) represents a transient equation that allows for the analysis of the dynamics in the inlet section of a three-phase separator. However, when we are interested in the steady-state behavior, the transient term on the left side of Eq. (7) can be ignored since it becomes zero. Another potential simplification for the model is applicable in systems where the droplet size distribution rapidly reaches an equilibrium state because of swift dynamics. If the transient time scale of droplet size evolution is orders of magnitude smaller than the residence time of the inlet section, the last term on the right-hand-side side of Eq. (7) related to inflow/outflow becomes insignificant. In other words, if the geometric design of

the inlet section allows for a residence time long enough to allow the coalescence and breakage mechanisms to equilibrate in the flow field of the inlet section, then the inlet drop size distributions from the upstream are irrelevant. As a result, we can assume that the system's behavior becomes independent of the inlet droplet size distribution, and the equilibrium distribution can be achieved by solving the steady-state form of Eq. (7) while ignoring the last term. For the calculation of the transient time scale of droplet size evolution, we refer the reader to Assar and Grimes (2022).

## 2.2. Separation section

As mentioned, the separation section is the region downstream of the calming baffle. Here, the flow is less turbulent, which enhance droplets coalescence and settle due to gravity. The zone's model is composed of various sub-models. We introduced transient models to maintain the generality of the overall models. However, during the derivation process, we relied on quasi-steady state assumptions for both flow rate and level. The model for this zone is described in the following sections.

### 2.2.1. Geometrical averaging

Circular segments are formed by the liquid levels in a horizontal cylindrical separator as depicted in Fig. 1c. The wetted perimeter ( $P_i$ ), area ( $A_i$ ), and volume ( $V_i$ ) of the liquid segments formed for water-continuous ( $wc$ ) and oil-continuous ( $oc$ ) layers can be calculated as follows:

$$P_{wc} = \theta_{wc} R \quad (16)$$

$$P_{oc} = \theta_{oc} R - P_{wc} \quad (17)$$

$$A_{wc} = \frac{\theta_{wc} R^2}{2} - \frac{(R - l_{wc}) w_{wc}}{2} \quad (18)$$

$$A_{oc} = \frac{\theta_{oc} R^2}{2} - \frac{(R - l_{oc}) w_{oc}}{2} - A_{wc} \quad (19)$$

$$V_i = A_i L_{e,i} \quad (20)$$

The segment width ( $w_i$ ) and segment angle ( $\theta_i$ ) are calculated as below:

$$w_i = 2\sqrt{(2Rl_i - l_i^2)} \quad (21)$$

$$\theta_i = 2\arccos\left(\frac{R - l_i}{R}\right) \quad (22)$$

where  $l_i$  is the liquid level from bottom of the separator,  $L_{e,i}$  is the effective separation section length (distance from the calming baffle to the outlet nozzle for the water-continuous layer and distance from the calming baffle to overflow weir for the oil-continuous layer; however, an average of both can be used for the simulation), and  $R$  is the radius of the separator.

Treating a three-phase separator as a 3D object, especially when coupled with a PBE, results in a computationally expensive problem due to the high dimensionality. Transient analysis of this system involves dealing with five different dimensions. To simplify the problem, we only consider the relevant dimensions for droplet transport, which are the axial and vertical directions. This approach follows the method proposed by Backi et al. (2018). In this approach, we disregard the outlet nozzle effect, which would require a 3D modeling approach.

To achieve this, we need to take the average of the dimensions and transform the geometry of the circular segments into rectangles. For the water-continuous layer (also for oil-continuous layer if no vapor phase is present in the system), the key factor in this mapping is averaging the vertical distance from the bottom/top (which are curved) to the interface. For oil-continuous layer, the height of the layer was kept equal to the difference between the levels and the width was calculated by

keeping the cross-section area constant. Accordingly, the circular segments are transformed to rectangles as shown in Fig. 1c. with the following widths and heights:

$$H_{wc} = \frac{A_{wc}}{w_{wc}} \quad (23)$$

$$H_{oc} = l_{oc} - l_{wc} \quad (24)$$

### 2.2.2. Velocity profiles

In the majority of industrial three-phase separators, the flow is typically slightly turbulent. When considering the flow of liquids with a free liquid surface, the transition to turbulent flow regime occurs at approximately Reynolds number of 1500 (Bird et al., 2006). This transition Reynolds number, calculated at the inlet of the separation sections, can serve as a criterion for selecting flow regime and consequently appropriate model solver. The Reynolds number is defined as:

$$Re_i(z, t) = \frac{\rho_i(z, t) \bar{u}_{z,i}(z, t) d_{h,i}(t)}{\mu_i(z, t)} \quad (25)$$

where  $\bar{u}_{z,i}$  is the average axial velocity; the dispersion density can be calculated by using volume fraction weighted density as suggested by Schumann (2016) and dispersion viscosity is estimated according to Pal and Rhodes (1989):

$$\rho_i(z, t) = \phi_w(z, t) \rho_w + \phi_o(z, t) \rho_o \quad (26)$$

$$\mu_i(z, t) = \mu_c \left[ 1 + \frac{\phi_d(z, t)/K_{PR,i}}{1.1884 - \phi_d(z, t)/K_{PR,i}} \right]^{2.5} \quad (27)$$

The parameter  $K_{PR,i}$  needs to be determined experimentally for the emulsion under investigation.

In Eq. (25),  $d_{h,i}(t)$  is the hydraulic diameter of the dispersion layer and defined as below:

$$d_{h,i}(t) = 4 \frac{A_i(t)}{P_i(t)} \quad (28)$$

In Eq. (28), the inclusion of time functionality serves to extend the model's applicability to scenarios involving transient change in the liquid level. For turbulent cases, a plug flow assumption has been used in the model. Accordingly, the average axial velocity for each layer can be calculated as below:

$$u_{z,i}(z, t) = \frac{Q_i(z, t)}{A_i(t)} \quad (29)$$

It is important to emphasize that the flow rates,  $Q_i$ , are no longer assumed to be constant due to the quasi-steady state assumption. Instead, it can now vary with time and axial location. The time dependence arises from transient variations in the inlet flow rate and interfacial coalescence rate. Similarly, the axial dependence is introduced through the interfacial coalescence, which leads to changes in the flow rate of the dispersion layer.

For laminar flow regime, by changing the problem to a 2D geometry, a simplification of the momentum and continuity equations can be

achieved using the below assumptions:

- The velocity profile is assumed to be fully developed along the length of the separator. The end effects such as that of the outlet nozzle are considered to be negligible. Therefore, the fluid velocity in  $x$  and  $y$  directions are zero.
- It is assumed that any transient changes in the flow rates and liquid levels occur slowly enough so that the velocity profiles can rapidly establish themselves at any given time. This assumption implies that the velocity profiles adjust quickly in response to changes in flow rates and liquid levels, allowing for a quasi-steady state behavior in the system.
- The changes of the flow rates in the axial direction are small enough that the velocity profiles can rapidly establish themselves at any location by quickly responding to flow rate changes.
- The velocity differences between the two layers are assumed to be sufficiently small. This assumption ensures that the interface between the layers remains undisturbed, eliminating the need for complex 3D modeling to account for possible vorticity.
- At the interfaces between the liquid–solid and liquid–liquid phases, it is assumed that there is no slip velocity.
- The assumption is made that the shear stress at the gas–liquid interface is negligible.
- The density and viscosity of the mixture are assumed to be uniform along the vertical axis ( $y$ ) within each dispersion layer. In practical terms, average values of mixture density and viscosity over the  $y$ -axis are used, with the understanding that these properties may vary with time and along the  $z$ -axis.

By employing the aforementioned assumptions, it is possible to derive an analytical expression for the laminar profile through the solution of the momentum and continuity equations. For a more comprehensive understanding of the detailed description and derivation, interested readers are encouraged to refer to the [Supplementary material](#) section in this paper.

$$u_{z,wc}(y_{wc}, z, t) = 3(H_{wc} - y_{wc}) \frac{C_{1,wc}(H_{wc} - y_{wc}) + C_{2,wc}}{C_{3,wc}} \quad (30)$$

$$u_{z,oc}(y_{oc}, z, t) = 3 \frac{C_{1,oc}(y_{oc} + H_{wc})^2 + C_{2,oc}(y_{oc} + H_{wc}) + C_{3,oc}}{C_{4,oc}} \quad (31)$$

where the coefficients in Eqs. (30), (31) are as below:

$$C_{1,wc}(z, t) = 3Q_{oc}\mu_{wc}W_{wc}H_{wc}^2 - 2Q_{wc}\mu_{wc}W_{oc}H_{oc}^2 - 6Q_{wc}\mu_{oc}W_{oc}H_{oc}H_{wc} \quad (32)$$

$$C_{2,wc}(z, t) = 6Q_{wc}\mu_{oc}W_{oc}H_{oc}H_{wc}^2 + 4Q_{wc}\mu_{wc}W_{oc}H_{oc}^2H_{wc} - 2Q_{oc}\mu_{oc}W_{wc}H_{wc}^3 \quad (33)$$

$$C_{3,wc}(z, t) = W_{oc}W_{wc}H_{oc}H_{wc}^3(4\mu_{wc}H_{oc} + 3\mu_{oc}H_{wc}) \quad (34)$$

$$C_{1,oc}(z, t) = 3Q_{wc}\mu_{wc}W_{oc}H_{oc} - 2Q_{oc}\mu_{wc}W_{wc}H_{wc} \quad (35)$$

$$C_{2,oc}(z, t) = 4Q_{oc}\mu_{wc}W_{wc}H_{wc}^2 + 4Q_{oc}\mu_{wc}W_{wc}H_{oc}H_{wc} - 6Q_{wc}\mu_{wc}W_{oc}H_{oc}^2 - 6Q_{wc}\mu_{wc}W_{oc}H_{oc}H_{wc} \quad (36)$$

$$C_{3,oc}(z, t) = 2Q_{wc}\mu_{wc}W_{oc}H_{oc}^3 - 2Q_{oc}\mu_{wc}W_{wc}H_{wc}^3 + Q_{oc}\mu_{oc}W_{wc}H_{oc}H_{wc}^2 - 4Q_{oc}\mu_{wc}W_{wc}H_{oc}H_{wc}^2 + 3Q_{wc}\mu_{wc}W_{oc}H_{oc}H_{wc}^2 + 6Q_{wc}\mu_{wc}W_{oc}H_{oc}^2H_{wc} \quad (37)$$



$$C_{4,oc}(z, t) = W_{oc} W_{wc} H_{oc}^2 H_{wc} (4\mu_{wc} H_{oc} + 3\mu_{oc} H_{wc}) \quad (38)$$

It is worth emphasizing that due to the quasi-steady state assumption, the volumetric flow rates,  $Q_{oc}$  and  $Q_{wc}$ , are now allowed to vary with both time and axial location. On the other hand, the liquid levels and widths,  $H_{oc}$ ,  $H_{wc}$ ,  $W_{oc}$  and  $W_{wc}$  solely vary with time. Additionally, the dispersion viscosities,  $\mu_{oc}$  and  $\mu_{wc}$  need to be calculated taking into account the dispersed phase average volume fraction in the vertical direction. Since this value can change with time and axial location, the viscosities should be updated accordingly at each time and axial location in order to more accurately capture the behavior of the system.

### 2.2.3. Dispersion model

In instances where no coalescing unit (whether electrical or non-electrical) is utilized within the separator, the balance equation encompasses binary coalescence, droplet breakage, gravity-driven transport, and axial velocity transport. Based on these observations, a comprehensive balance equation for the dispersion layers can be expressed as follows:

$$\begin{aligned} \frac{\partial f_{SS,i}(r_i, y_i, z, t)}{\partial t} = & -\frac{\partial}{\partial z} \left[ u_{z,i}(y_i, z, t) f_{SS,i}(r_i, y_i, z, t) \right] \\ & -\frac{\partial}{\partial y_i} \left[ u_{y,i}(r_i, y_i, z, t) f_{SS,i}(r_i, y_i, z, t) \right] \\ & +\frac{\partial}{\partial y_i} \left[ D_{e,i}(r_i, y_i, z, t) \frac{\partial f_{SS,i}(r_i, y_i, z, t)}{\partial y_i} \right] \\ & +R_{bb,i}(r_i, y_i, z, t) - R_{bd,i}(r_i, y_i, z, t) \\ & +R_{cb,i}(r_i, y_i, z, t) - R_{cd,i}(r_i, y_i, z, t) \\ & \forall r_i |_{0 \leq r_i \leq \infty}, y_i |_{0 < y_i < H_i(t)}, z |_{0 < z \leq L_e}, t |_{0 < t \leq t_f} \end{aligned} \quad (39)$$

It worth noting that the inclusion of the diffusive term in Eq. (39) is crucial to account for the potential existence of a dense pack layer within the system. The detailed explanation of this term can be found in [Section 2.2.7](#). The birth and death rates arising from the coalescence and breakage terms are defined as follows:

$$R_{bb,i}(r_i, y_i, z, t) = \int_{r_i}^{\infty} 2\gamma_{t,i}(r_i', z, t) \beta(r_i', r_i) f_{SS,i}(r_i', y_i, z, t) \frac{r_i'^3}{r_i^3} dr_i' \quad (40)$$

$$R_{bd,i}(r_i, y_i, z, t) = \gamma_{t,i}(r_i, z, t) f_{SS,i}(r_i, y_i, z, t) \quad (41)$$

$$\begin{aligned} R_{cb,i}(r_i, y_i, z, t) = & \left( \frac{3}{4\pi} \right) \int_0^{\frac{r_i}{\sqrt{2}}} \kappa_{SS,i}(r_i', r_i'', y_i, z, t) \times \\ & f_{SS,i}(r_i', y_i, z, t) f_{SS,i}(r_i'', y_i, z, t) \frac{r_i'^5}{r_i^3 r_i'^{5/2}} dr_i' \end{aligned} \quad (42)$$

$$R_{cd,i}(r_i, y_i, z, t) = \left( \frac{3}{4\pi} \right) f_{SS,i}(r_i, y_i, z, t) \int_0^{\infty} \kappa_{SS,i}(r_i', r_i, y_i, z, t) f_{SS,i}(r_i', y_i, z, t) \frac{1}{r_i^3} dr_i' \quad (43)$$

When it comes to the birth and death rates associated with breakage, only the break-up caused by turbulent fluctuations same as [section 2.1.2](#) is considered (i.e., Eqs. (12) and (13)). However, in the case of laminar conditions, there are other potential mechanisms to consider, such as break-up caused by viscous shear stress ([Liao et al., 2015](#)) which is ignored in this model. Therefore, breakage terms are only considered in the model when the flow regime is turbulent. Accordingly, the computational program employs the appropriate solver based on the detected flow regime. Also, the coalescence terms mentioned in the equations above are elaborated and discussed in detail in [section 2.2.8](#).

To determine the turbulent breakage rate, the turbulent energy dissipation rate can be computed using the following equation ([Bin Ismail, 2021](#)).

$$\varepsilon_i(z, t) \approx 0.16 Re_i(z, t)^{2.75} \left( \frac{\nu_i(z, t)}{d_{h,i}(t)^4} \right) \quad (44)$$

In the given equation,  $\nu$  stands for kinematic viscosity. It is essential to emphasize that  $\nu$  and  $Re$  should be computed as an average across the vertical direction. Furthermore,  $d_h$  represents the hydraulic diameter and can be calculated using Eq. (28).

The balance equation (Eq. (39)) is governed by the following boundary conditions.

$$\begin{aligned} & u_{y,i}(r_i, y_i, z, t) f_{SS,i}(r_i, y_i, z, t) \\ & - D_{e,i}(r_i, y_i, z, t) \frac{\partial f_{SS,i}(r_i, y_i, z, t)}{\partial y_i} = 0 \\ & \text{at } y_i = H_i(t), \forall r_i |_{0 \leq r_i \leq \infty}, z |_{0 < z \leq L_e}, t |_{0 < t \leq t_f} \end{aligned} \quad (45)$$

$$\begin{aligned} & u_{y,i}(r_i, y_i, z, t) f_{SS,i}(r_i, y_i, z, t) \\ & - D_{e,i}(r_i, y_i, z, t) \frac{\partial f_{SS,i}(r_i, y_i, z, t)}{\partial y_i} \\ & = u_{ic,i}(r_i, z, t) f_{SS,i}(r_i, y_i, z, t) \text{ at } y_i = 0, \\ & \forall r_i |_{0 \leq r_i \leq \infty}, z |_{0 < z \leq L_e}, t |_{0 < t \leq t_f} \end{aligned} \quad (46)$$

Eq. (45) simply expresses that the net droplet flux is zero at  $H_i$  (top boundary for the oil-continuous and bottom boundary for the water-continuous). On the other hand, Eq. (46) states that the total outlet droplet flux at the interface between the layers is equal to the flux resulting from the interfacial coalescence for each respective layer.

$$\begin{aligned} f_{SS,i}(r_i, y_i, z, t) = f_{IS,i}(r_i, t) \text{ at } z = 0, \\ \forall r_i |_{0 \leq r_i \leq \infty}, y_i |_{0 \leq y_i \leq H_i(t)}, t |_{0 < t \leq t_f} \end{aligned} \quad (47)$$

Eq. (47) also states that the inlet distribution to the separation section is simply the one from the inlet section. The initial conditions are also as follows:

$$\begin{aligned} f_{SS,i}(r_i, y_i, z, t) = f_{SS,i,0}(r_i, y_i, z) \text{ at } t = 0, \\ \forall r_i |_{0 \leq r_i \leq \infty}, y_i |_{0 \leq y_i \leq H_i(t)}, z |_{0 \leq z \leq L_e} \end{aligned} \quad (48)$$

The moment properties employed for visualizing the simulation results are computed as follows:

$$\phi_{d,i}(y_i, z, t) = \int_0^{\infty} f_{SS,i}(r_i, y_i, z, t) dr_i \quad (49)$$

$$\mu_{r,i}(y_i, z, t) = \frac{1}{\phi_{d,i}(y_i, z, t)} \int_0^{\infty} r f_{SS,i}(r_i, y_i, z, t) dr_i \quad (50)$$

### 2.2.4. Flow rate model

The interfacial coalescence occurs at the interface where the two dispersed layers are in contact. Specifically, water droplets from the oil-continuous phase settle and reach the interface level, where they merge with the water-continuous layer. This integration leads to an increase in the volume flow rate and, consequently, the velocity of the water-continuous layer as well as a decrease in those of oil-continuous layer. A similar process takes place within the water-continuous layer. Therefore, it is essential to treat the two layers simultaneously in numerical simulations, as they are coupled and interdependent.

The convective flux for a droplet of size  $r$  in layer  $i$  at the interface can be written as below:

$$n_{ic,i}(r_i, t) = u_{ic,i}(r_i, z, t) f_{SS,i}(r_i, y_i, z, t) \Big|_{y_i=0} \quad (51)$$

where  $u_{ic,i}$  is the equivalent velocity at which the droplet of size  $r$  leaves the dispersion layer  $i$  by coalescing into the adjacent layer at the interface. This velocity can be calculated as below:

$$u_{ic,i}(r_i, z, t) = \frac{4r_i}{3t_{ic,i}(r_i, z, t)} \quad (52)$$

For a more in-depth understanding of the derivation of Eq. (52), interested readers can refer to the previous work (Assar et al., 2023). In this equation,  $t_{ic}$  represents the interfacial coalescence time, which denotes the duration for a droplet with size  $r$  in layer  $i$  to fully integrate with the adjacent layer after making contact with the interface. This term will be elaborated upon using a parallel film drainage model in section 2.2.9. By employing the following term (Eq. (52)), it becomes possible to calculate the total volumetric flow rate of the dispersed phase over the interface. Accordingly, the changes in the volumetric flow rate of layers are governed by the below equation:

$$\frac{dQ_{oc}(z, t)}{dz} = -\frac{dQ_{wc}(z, t)}{dz} = w_{wc}(t) \times \left( \int_0^\infty u_{ic,wc}(r_{wc}, z, t) f_{SS,wc}(r_{wc}, y_{wc}, z, t) \Big|_{y_{wc}=0} dr_{wc} - \int_0^\infty u_{ic,oc}(r_{oc}, z, t) f_{SS,oc}(r_{oc}, y_{oc}, z, t) \Big|_{y_{oc}=0} dr_{oc} \right) \quad (53)$$

$\forall z|_{0 < z \leq L_e}, t|_{0 < t \leq t_f}$

subject to the following boundary condition:

$$Q_i(z, t) = Q_{out,i}(t) \text{ at } z = L_e, \forall t|_{0 < t \leq t_f} \quad (54)$$

where  $Q_{out,i}$  is the outflow from the layer through the outlet nozzles. It is important to note that due to the quasi-steady-state assumption, any transient changes in this flow rate will immediately propagate and establish themselves along the entire length of the separation section.

### 2.2.5. Liquid level transient model

In the oil and gas industry, separators typically incorporate level control systems. However, certain subsea designs rely solely on gravity flow and lack level control mechanisms. In such cases, a more complex hydrodynamic analysis becomes necessary to calculate the liquid levels. When a level control is employed, the transient model for liquid levels can be derived by considering variations in the inflow and outflow of the equipment. The following equations can be utilized to account for transient changes in the liquid levels for water and oil continuous layers.

$$L_e \frac{dA_{oc}(t)}{dt} = Q_{IS,oc}(t) - Q_{out,oc}(t) + w_{wc}(t) \int_0^{L_e} \times \int_0^\infty u_{ic,wc}(r_{wc}, z, t) f_{SS,wc}(r_{wc}, y_{wc}, z, t) \Big|_{y_{wc}=0} dr_{wc} dz - w_{wc}(t) \int_0^{L_e} \times \int_0^\infty u_{ic,oc}(r_{oc}, z, t) f_{SS,oc}(r_{oc}, y_{oc}, z, t) \Big|_{y_{oc}=0} dr_{oc} dz \quad \forall t|_{0 < t \leq t_f} \quad (55)$$

$$L_e \frac{dA_{wc}(t)}{dt} = Q_{IS,wc}(t) - Q_{out,wc}(t) - w_{wc}(t) \int_0^{L_e} \times \int_0^\infty u_{ic,wc}(r_{wc}, z, t) f_{SS,wc}(r_{wc}, y_{wc}, z, t) \Big|_{y_{wc}=0} dr_{wc} dz + w_{wc}(t) \int_0^{L_e} \times \int_0^\infty u_{ic,oc}(r_{oc}, z, t) f_{SS,oc}(r_{oc}, y_{oc}, z, t) \Big|_{y_{oc}=0} dr_{oc} dz \quad \forall t|_{0 < t \leq t_f} \quad (56)$$

where  $Q_{IS,i}$  can be calculated using the Eqs. (1) and (2). Above Equations describe the transient change in the cross-section area of the dispersion layers; however, it is still possible to use the geometrical relations to derive transient equation for change in the layer's heights,  $H_{oc}$  and  $H_{oc}$ , which we are more interested in. The mentioned derivation is presented in the Supplementary material section. Also, the initial conditions for the liquid levels are as below:

$$H_i(t) = H_{0,i} \text{ at } t = 0 \quad (57)$$

At this point, we need to reiterate that the derivation of the level transient equations relies on the assumption of quasi-steady state, where flow quickly reaches a stable condition. Eqs. (55) and (56) highlight that the boundary of the independent vertical variable  $y$  is not constant. Consequently, this leads to a moving boundary problem, which has been addressed by employing a time-spatial transformation method presented in the Supplementary material section.

### 2.2.6. Droplet velocity

The slip velocity, which represents the difference between the velocity of the droplets and the continuous phase, depends on both the droplet size and the volume fraction of the dispersed phase. Various approaches exist for calculating the slip velocity. In our previous work Assar et al. (2023), we demonstrated that the slip velocity proposed by Kumar and Hartland (1985) yields better agreement with experimental data compared to the Richardson-Zaki model (Richardson and Zaki, 1954) and the slip velocity formulated using the drag coefficient by Behzadi et al. (2004). Moreover, the Kumar and Hartland slip velocity model remains valid across a wide range of volume fractions and Reynolds numbers. In this study, we employ the mentioned model as stated below:

$$0.53u_{s,i}^2 + \frac{12\mu_c}{r_i\rho_c}u_{s,i} + \frac{2r_i g(\rho_c - \rho_d)(1 - \phi_{d,i})}{3\rho_c(1 + 4.56\phi_{d,i}^{0.73})} = 0 \quad (58)$$

Solving the above equation yields the following equation for slip velocity:

$$u_{s,i}(r_i, y_i, z, t) = \left[ 128.16 \frac{\mu_c^2}{r_i^2 \rho_c^2} + 1.258 \frac{g r_i |\rho_c - \rho_d|}{\rho_c} \frac{(1 - \phi_{d,i}(y_i, z, t))}{(1 + 4.56\phi_{d,i}(y_i, z, t)^{0.73})} - 11.321 \frac{\mu_c}{r_i \rho_c} \right]^{0.5} \quad (59)$$

In sloped sections of a separator, where the angle between the axial direction and the horizontal axis is  $\delta$ , the gravitational acceleration constant ( $g$ ) should be adjusted to  $g \cos(\delta)$ . Having the slip velocity, the droplet velocity can be calculated as below:

$$u_{y,i}(r_i, y_i, z, t) = (1 - \phi_{d,i}(y_i, z, t)) u_{s,i}(r_i, y_i, z, t) \quad (60)$$

### 2.2.7. Effective diffusion

To address the potential formation of a dense packed layer, we have introduced an effective diffusion coefficient in Eq. (39). Drawing upon our prior research (Assar et al., 2023), we employ the following equation to determine this parameter:

$$D_{e,i}(r_i, y_i, z, t) = C_{0,i} u_{y,i}(r_i, y_i, z, t) \left( \frac{(\phi_{d,i}(y_i, z, t)/\phi_{m,i})^{0.23}}{(1 - \phi_{d,i}(y_i, z, t)/\phi_{m,i})^{1.29}} \right) \quad (61)$$

The utilization of the aforementioned effective diffusion in Eq. (39) ensures the conservation of the volume fraction within the range of 0 to  $\phi_{m,i}$ . In this study, a value of 0.9 is adopted for  $\phi_{m,i}$ , which represents the maximum allowable dispersed phase volume fraction. The specific value of  $\phi_{m,i}$  can vary based on two key factors: the standard deviation of the droplet size distribution and the degree of droplet deformation. The  $C_{0,i}$  is the model constant and has the functionality of interfacial tension and phase density difference, the numerical value of  $5.1 \times 10^{-4} m$  was considered for this parameter similar to the previous work (Assar et al., 2023).

### 2.2.8. Binary coalescence model

As mentioned earlier, the separation section of most industrial separators operates under turbulent flow regimes. In such conditions,

turbulence-induced coalescence and breakage mechanisms become dominant. However, in cases where laminar flow occurs, buoyancy-induced and velocity-gradient induced mechanisms become plausible for coalescence. To maintain the generality of the model, coalescence is considered as the sum of these mechanisms, as shown below:

$$\kappa_{SS,i}(r_i, r_i', y_i, z, t) = \omega_{t,i}(r_i, r_i', z, t)\psi_{t,i}(r_i, r_i', z, t) + \omega_{b,i}(r_i, r_i', y_i, z, t)\psi_{b,i}(r_i, r_i') \quad (62)$$

The first term can be computed using Eq. (9). In turbulent flow, even with a minimal dissipation rate, the turbulent term can significantly outweigh the buoyancy term. Hence, in practical terms, the buoyancy-driven coalescence can be disregarded for turbulent flow and its application is primarily limited to cases with low Reynolds numbers, corresponding to laminar flow regimes, or for simulating transient scenarios such as shutdown cases. The binary coalescence resulting from buoyancy forces is taken into account based on the approach proposed by Grimes (2012).

In Eq. (62), coalescence efficiency ( $\psi_b$ ) and collision frequency ( $\omega_b$ ) are defined as follows:

$$\omega_{b,i}(r_i, r_i', y_i, z, t) = k_{c3,i} \frac{K_B T}{6\mu_c} \frac{(r_i + r_i')^2}{r_i r_i'} \left[ 1 + Pe_{bc}(r_i, r_i', y_i, z, t) + 4.496(Pe_{bc}(r_i, r_i', y_i, z, t))^{1/3} \right] \quad (63)$$

where  $K_B$  is the Boltzmann constant,  $T$  is the absolute temperature,  $k_{c3,SS,i}$  is a tuning parameter for the model, and  $Pe_{bc}$  is droplet pair Peclet number defined as below:

$$Pe_{bc}(r_i, r_i', y_i, z, t) = \frac{6\pi\mu_c}{K_B T} r_i r_i' |u_{s,i}(r_i, y_i, z, t) - u_{s,i}(r_i', y_i, z, t)| \quad (64)$$

where  $u_{s,i}$  is the droplet slip velocity and can be calculated using Eq. (59).

The coalescence efficiency is defined by the following equation.

$$\psi_{b,i}(r_i, r_i') = \exp(-t_{bc}(r_i, r_i')) \quad (65)$$

where  $t_{bc}$  denotes the time of binary coalescence, as indicated by the subsequent equation.

$$t_{bc,i}(r_i, r_i') = \frac{1.046}{k_{c4,i}} \frac{\mu_c |\rho_d - \rho_c| g}{\sigma^2 B^2} \left[ \frac{r_i r_i'}{r_i + r_i'} \right]^{9/2} \quad (66)$$

where  $\sigma$  is interfacial tension,  $B$  is the Hamaker constant, and  $k_{c4,SS,i}$  is another tuning factor.

### 2.2.9. Interfacial coalescence

According to Eq. (52), the interfacial coalescence time ( $t_{ic,i}$ ) serves as a key factor for determining the interfacial coalescence velocity and, consequently, the interfacial coalescence rate. The interfacial coalescence time was derived by Hahn and Slattery (1985), who introduced it to analyze the coalescence of a single bubble at a gas-liquid interface. Building upon this, Grimes (2012) later applied a comparable formulation to investigate the interfacial coalescence of a single droplet at a liquid-liquid interface as below:

$$t_{ic,i}(r_i) = 1.046 \frac{\mu_c |\rho_d - \rho_c| g}{\sigma^2 B^2} r_i^{9/2} \quad (67)$$

Expressed by Eq. (67), the buoyancy force acting upon an isolated stationary droplet at an interface is given by:

$$F_{drop}(r_i) = \frac{4\pi}{3} |\rho_d - \rho_c| g r_i^3 \quad (68)$$

When dealing with a dense packed layer (DPL), the droplets come into contact, leading to an increased force due to the stack of droplets upon one another. In such a scenario, the incremental volume of the droplets confined within a closely-knit arrangement of densely packed droplets over the incremental length of  $dz$  can be obtained using the below equation:

$$dV_{i,DPL}(z, t) = w_{wc}(t) dz \int_0^{y_{i,DPL}(z,t)} \phi_{d,i}(y_i, z, t) dy_i \quad (69)$$

The force exerted by that specific section of the DPL onto the interface can be calculated by considering the difference between the gravitational force and the buoyant force for a static condition, as shown in the following equation:

$$dF_{i,DPL}(z, t) = |\rho_d - \rho_c| g dV_{i,DPL}(z, t) \quad (70)$$

Dividing the incremental force by the corresponding incremental surface

area ( $w_{wc}(t)dz$ ), the pressure originating from the DPL and applied onto the interface is derived as follows:

$$P_{i,DPL}(z, t) = |\rho_d - \rho_c| g \int_0^{y_{i,DPL}(z,t)} \phi_{d,i}(y_i, z, t) dy_i \quad (71)$$

In Eq. (71),  $y_{i,DPL}$  is the DPL thickness. This parameter can be calculated by considering critical volume fraction ( $\phi_{cr,i}$ ) at which droplets make contact with each other and depends on the distribution of droplet sizes (Antonio García and Fernando Betancourt, 2019). According to the findings of Ruiz and Padilla (1996), they determined the value of this parameter to be approximately 0.53 for lower inlet values of the dispersed phase volume fraction. Conversely, for instances involving higher inlet volume fractions, the critical volume fraction was adopted as the inlet volume fraction.

For enhanced mathematical tractability, Eq. (71) can be reorganized into the subsequent expression:

$$P_{i,DPL}(z, t) = |\rho_d - \rho_c| g \int_0^{H_i(t)} \text{heaviside}(\phi_{d,i}(y_i, z, t) - \phi_{cr,i}) \phi_{d,i}(y_i, z, t) dy_i \quad (72)$$

Likewise, the force stemming from the height of the DPL, applied to a droplet with a size denoted as  $r_i$  that touches the liquid-liquid interface, is approximated by multiplying the DPL pressure by the characteristic area of the droplet ( $\pi r_i^2$ ):

$$F_{i,DPL}(r_i, z, t) = \pi |\rho_d - \rho_c| g r_i^2 \times \int_0^{H_i(t)} \text{heaviside}(\phi_{d,i}(y_i, z, t) - \phi_{cr,i}) \phi_{d,i}(y_i, z, t) dy_i \quad (73)$$

When dealing with a DPL, the force calculated using Eq. (73) significantly outweighs the force of a single droplet. Consequently, the force expression can be generalized by straightforwardly summing the two terms as follows:

$$F(r_i, z, t) = F_{drop}(r_i) + F_{DPL}(r_i, z, t) \quad (74)$$

It is notable that for practical purposes, we can simply ignore the first



term in Eq. (74).

By adapting the squeezing force in accordance with Eq. (74), the resulting interfacial coalescence time takes on the following form:

$$t_{ic,i}(r_i, z, t) = \frac{0.25}{k_{cs,ss,i}} \frac{\mu_c F(r_i, z, t)}{\sigma^2 B_2^2} r_i^{3/2} \quad (75)$$

where  $k_{cs,ss,i}$  represents a tuning parameter to handle non-idealities such as droplet deformation.

As per Eqs. (74) and (75), during the initial stages when the DPL has not yet developed, the interfacial coalescence rate is governed by single droplet buoyancy force, yielding a relatively low coalescence rate that leads to droplet accumulation and the eventual formation of the DPL. However, once the volume fraction crosses the critical threshold, at which the droplets come into close contact, DPL force takes charge of the coalescence rate dynamics, resulting in a different behavior.

### 3. Numerical analysis

The droplet size coordinates for the dispersed phases in both the water-continuous and oil-continuous layers ( $r_{oc}$  and  $r_{wc}$ ) were discretized using two separate grids. The same grids for the internal domain were utilized to discretize both inlet and separation sections. The study utilized the orthogonal collocation technique, as described by Villadsen and Michelsen (1978), in spectral-element framework to discretize the droplet size coordinate. Five elements were used for this purpose with elements' boundaries selected according to inlet droplet size distribution and estimated equilibrium distribution. Additionally, same number of collocation points were used for all the elements.

The finite volume method (FVM) was employed with equidistant cells to discretize the spatial coordinates ( $z$ ,  $y_{oc}$  and  $y_{wc}$ ) for transient solution of the problem. In this context, a structured mesh featuring equidistant cells in both width and height was employed. For the steady-state conditions, FVM discretization was only applied for the vertical coordinate while ODE solvers were implemented for the axial coordinate.

To handle the advection terms, the MUSCL technique described by Dale Anderson et al. (2020) was used. Central differencing was used to approximate the diffusion terms in the equations.

Further information regarding grid generation and the truncation of

the internal domain as well as spatial coordinate discretization is available in Assar et al. (2023).

Two different computational solvers were developed to handle steady-state and transient conditions. For transient conditions, the internal and spatial coordinates were discretized as described. Subsequently, a system of ordinary differential equations (ODEs) with respect to time derivatives was formed. To solve this system, the adaptive Gear's backward differentiation scheme, introduced by Gear in (1971), was employed. The adaptive nature of the scheme allows for efficient and accurate integration of the ODEs over time, adjusting the time step size as necessary to maintain stability and accuracy.

On the other hand, for the steady-state solver, the internal coordinates ( $r_{oc}$  and  $r_{wc}$ ) and the vertical coordinates ( $y_{oc}$  and  $y_{wc}$ ) were discretized. The subsequent system of ODEs, now with axial coordinate derivatives, was then integrated using Gear's method.

It is important to highlight that the mentioned approach may not be applicable for cases with laminar flow since the velocity is zero at the solid-liquid interface. Consequently, the term involving the axial derivative at  $y_{wc} = H_{wc}$  for the water-continuous phase becomes zero. Alternatively, for such cases, a transient simulation can be employed with an extended simulation time to allow the system to reach a steady-state condition.

Another crucial consideration pertains to ensuring that the droplet's equivalent interfacial coalescence velocity ( $u_{ic}$ ) remains constrained within the bounds of the sedimentation velocity ( $u_y$ ) at interface, thereby preventing the emergence of unrealistic numerical results.

To assess the accuracy and reliability of the computations, the numerical imbalances in the systems was calculated and observed during the simulations. Furthermore, the effect of grid refinement was examined as a means to ensure the accuracy of the numerical solution by increasing the resolution of the computational grids. More details regarding the numerical imbalances are presented in the Supplementary material section.

### 4. Experimental section

Skjefstad et al. introduced the Multiple Parallel Pipe Separator (MPPS) as a novel design for bulk oil-water separation (Skjefstad and Stanko, 2018, 2019; Skjefstad et al., 2020). This design incorporates multiple parallel pipes, resulting in improved settling times and a more

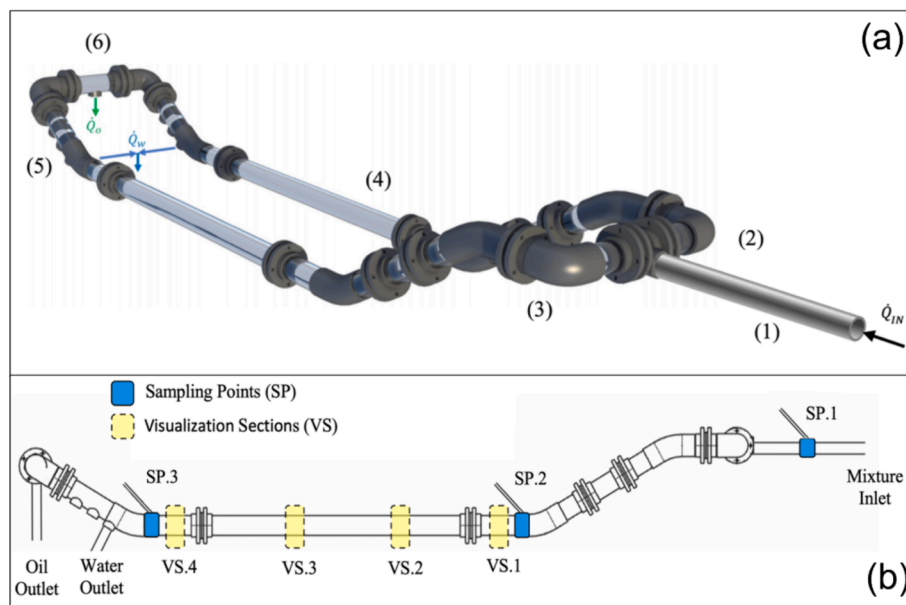


Fig. 2. (a) 3D model of MPPS, (b) side view of MPPS including inlet and outlets connections, sampling points, and visualization sections (Asaadian and Stanko, 2023).

compact, modular, and adaptable separator compared to existing subsea separator design (Skjefstad et al., 2020). Skjefstad constructed a prototype and conducted experiments, examining the impact of different design parameters on separation efficiency, as well as the influence of surfactants and inlet choking on the performance of the separator. Following this, Asaadian performed comprehensive studies on the performance (Asaadian et al., 2022; Asaadian and Stanko, 2023). In this work, the same MPPS setup is utilized to evaluate the separation process in pipes and investigate the effect of water-cut and flow rate on separation efficiency.

Fig. 2a showcases the components of the prototype MPPS, which include:

- (1): Tangential Intake: This component utilizes centrifugal forces to generate pre-separation. The heavier phase (salt water) is directed towards the pipe wall, while the lighter phase (oil) is directed towards the center.
- (2): Internal Device: Positioned in the elbow immediately downstream of the T-section, this device facilitates the transition from annular flow to a stratified regime. Additionally, the T-junction divides the inlet stream into two branches.
- (3): Descending Pipe Section: incorporated for two purposes, separating gas through extraction points on the top (not used in the current study) and perform pre-separation and establish a stratified layer upstream of the horizontal section.
- (4): Horizontal Section: This section spans 3.5 m in length and has an internal diameter of 150.6 mm. In this segment, the primary liquid-liquid separation occurs.
- (5): Ascending Pipe Section: outlet points are in this section. A water-rich stream is extracted near the bottom of the pipe, while the oil-rich stream continues to flow towards its outlet nozzle.
- (6): Oil-rich outlet nozzle.

In the mathematical analysis and conducted simulations that follow, only the descending pipe section and horizontal section are considered.

Furthermore, piping and instrumentation diagram of the experimental set-up together with more detailed description of the process is provided in the [Supplementary material](#).

Fig. 2b presents three designated sampling points positioned at the inlet pipe, as well as the beginning and end of the horizontal section. These sampling points are strategically placed to extract samples from the dispersion layer, enabling the measurement of the water cut within the emulsion layer. [Supplementary material](#) showcases the utilization of the Mettler Toledo PVM V819 probe, which captures microscopic images from the emulsion layer through the designated sampling points. These images allow for real-time droplet size distribution measurement of the dispersion layers. Furthermore, four visualization sections are demarcated along the transparent horizontal pipe, facilitating the assessment of water and oil layer thickness using cameras.

The experiments utilized distilled water with 3.4 wt% NaCl for the water phase, and mineral oil (Exxsol D60) with added surfactant for the oil phase. The surfactant was incorporated into the mineral oil at a concentration of 400 ppm to imitate the separation behavior of crude oil-water emulsions. The amount of crude oil added was determined based on bottle tests, ensuring a similar separation time as the crude oil emulsion used in field operations at its operating temperature of 60 °C. Detailed procedures for fluid preparation and physio-chemical property

measurements can be found in [Asaadian and Stanko \(2023\)](#). The physical properties of the fluids are provided in [Table 1](#).

The emulsion exhibited an inversion point at approximately 30 vol% water-cut. For water-cuts below this point, there is a transition in the continuous phase from water to oil. The study also encompassed an analysis of emulsion viscosities. A correlation was fine-tuned for the studied emulsion using the Pal Rhodes equation (Eq. (27)), as elaborated upon in [section 2.2.2](#). Accordingly the model parameter  $K_{PR,wc}$  was experimentally determined to have a value of 0.86 ([Asaadian and Stanko, 2023](#)).

Additionally, the droplet size distribution (DSD) of the separated phases was measured at the entry point of the horizontal section for all the cases examined. These DSDs are detailed in the [Supplementary materials](#) section.

The water-cuts (volumetric flow rate of water to total volumetric flow rate) of the inlet oil and water feed streams were determined through the following calculation:

$$\alpha_i = \frac{\rho_i - \rho_o}{\rho_w - \rho_o} \quad (76)$$

where  $i$  denotes the inlet stream ( $oi$ : oil inlet stream,  $wi$ : water inlet stream). Additionally, the inlet stream water cut can be determined using the following equation.

$$\alpha = \frac{\alpha_{oi}Q_{oi} + \alpha_{wi}Q_{wi}}{Q_{oi} + Q_{wi}} \quad (77)$$

During the experiments, the water cut in the water stream is nearly 100 %, and the oil line contains almost no water. However, it is important to consider the potential presence of oil in the water stream and water in the oil stream due to inadequate separation in the storage tank. The water-cut of the outlet stream as well as the separation efficiency were measured at fixed extraction ratio, defined as follows:

$$ER_w = \frac{Q_{wo}}{Q_{wi}} \quad (78)$$

where  $Q_{wo}$  is outlet water stream flow rate. The separation efficiency is calculated by dividing the flow rate of extraction water by the maximum possible flow of water that can be separated at a specified ER. The equation is as follows:

$$SE_w = \frac{\alpha_{wo}Q_{wo}}{ER_w\alpha(Q_{oi} + Q_{wi})} \quad (79)$$

## 5. Results and discussion

The analysis of the experimental data was carried out through the utilization of the model. To enhance the numerical manageability of the model for the purpose of parameter estimation, a set of assumptions and considerations have been incorporated, taking into account the experimental observations. The following is a summary of these assumptions and considerations:

- All experiments feature a single poly-dispersed layer, where water acts as the continuous phase. This choice is driven by the fact that the average oil fraction in all the experiments consistently remains below the inversion point. Consequently, the dispersion model is exclusively applied to the water-continuous layer, and it is inferred that the top layer consists of purely oil. Under this premise, it is also postulated that at the inlet of the separation section, the flow rate of the water-continuous phase aligns with the overall inlet flow of the separator.
- Due to the turbulent nature of the flow across all experiments ( $2000 < Re < 10^5$ ), solely turbulent coalescence and breakage phenomena were considered, with the influence of buoyancy-induced coalescence deemed negligible. Additionally, given the consistently

**Table 1**  
Fluid properties.

Fluid	Water	Oil
Density [kg/m <sup>3</sup> ]	1020.7	787.45
Viscosity [cP]	0.99	1.31
Temperature [degC]		20
Interfacial tension [mN/m]		29

turbulent flow conditions, a simplifying assumption of plug flow was adopted.

- Our analysis of the eddy diffusivity magnitude confirms that axial dispersion can be safely neglected in the studied system.
- The DSD is measured at the inlet of the separation section, leading to the omission of the inlet section in the model's scope. The DSD curves are presented in the [Supplementary material](#) section.
- An assumption is made that the liquid level remains uniform along the separation section, irrespective of its sloped or non-sloped segments. In practice, an average value derived from both inlet and outlet levels was employed in the model. The level profiles are presented in the [Supplementary](#) section.
- Steady-state condition prevail. Notably, all measurements were conducted subsequent to the establishment of these steady-state conditions.

As described, the separation section comprises both a sloped and a horizontal segment. For model development, distinct dispersion models were formulated for these two sections, namely the descending pipe and the horizontal sections. These two sections differ in the determination of droplet sedimentation velocity. Notably, the outlet DSD and flow rate from the sloped section are adopted as the inlet boundary conditions for the subsequent horizontal section. All the conducted simulations include

both sections.

Six cases were experimentally studied to evaluate the effect of different parameters on the water separation efficiency namely, inlet water-cut (30 and 50 %) and flow rate (300, 500, and 700 L/min). All the experiments were conducted at extraction rate equal to 90 %.

As the first level of analysis, all the tuning parameters in the model were set to unity. The Retarded Hamaker constant holds significance in this model as another key parameter. Typically, this parameter should be determined experimentally; however, due to the absence of experimental data for the Hamaker constant in the studied system, we opted to treat it as a tuning parameter. Initially, we estimated the Retarded Hamaker constant using Eq. (75) and the shrink rate (slope at which DPL thickness changes after forming) measured at the point the emulsion layer is completely established. This rough estimation involved assuming an average droplet size for the DPL emulsion and calculating the Hamaker constant to get the DPL's shrinking rate via Eq. (75). This estimated value served as an initial guess, undergoing further refinement through a comparison of simulation results and the experimental data on water separation efficiency. Ultimately, a numerical value of  $7.3 \times 10^{-28} \text{ N/m}^2$  was fine-tuned for this parameter.

The model results for dispersed phase volume fraction and average droplet size of water-continuous layer are presented in [Figs. 3 and 4](#) for all the studied cases.

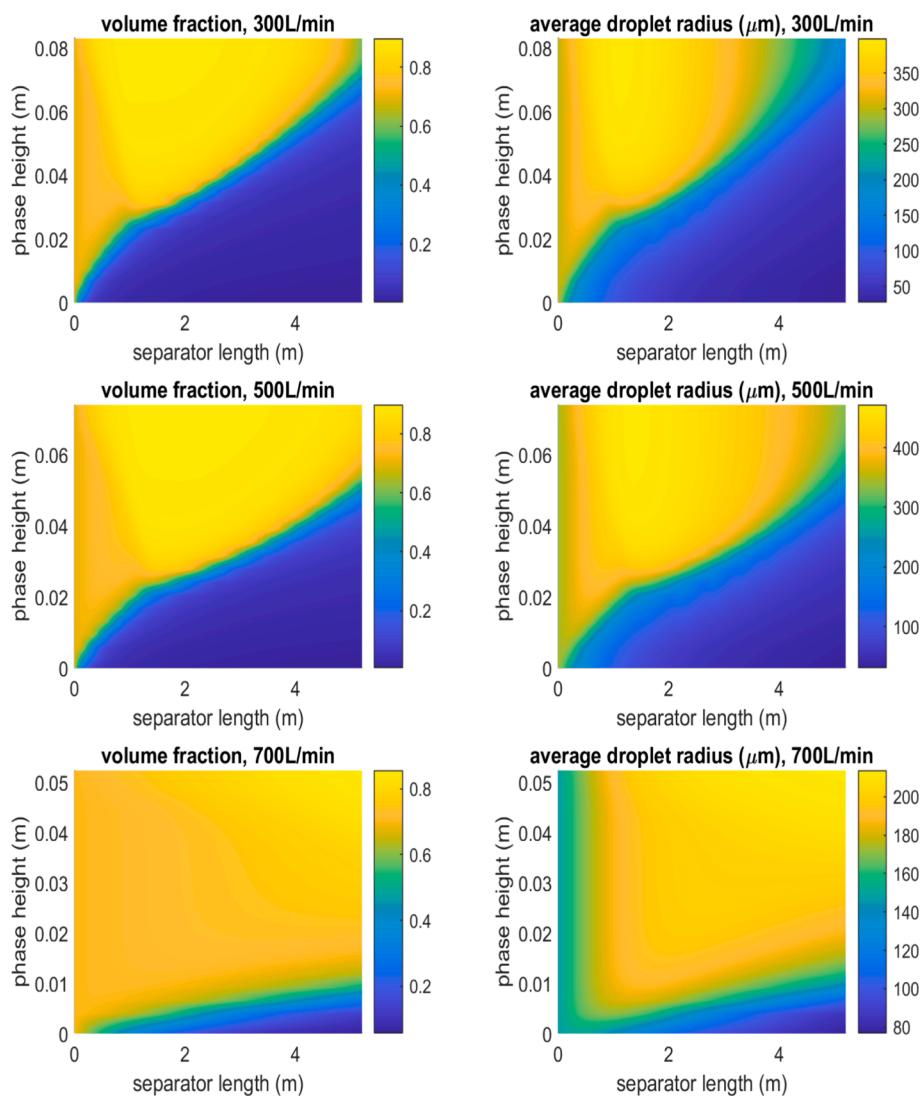


**Fig. 3.** Simulation results for oil volume fraction (left) and average droplet size (right) for WC = 30 % and varying total liquid volumetric flow rates (300, 500, 700 L/min from top to bottom).

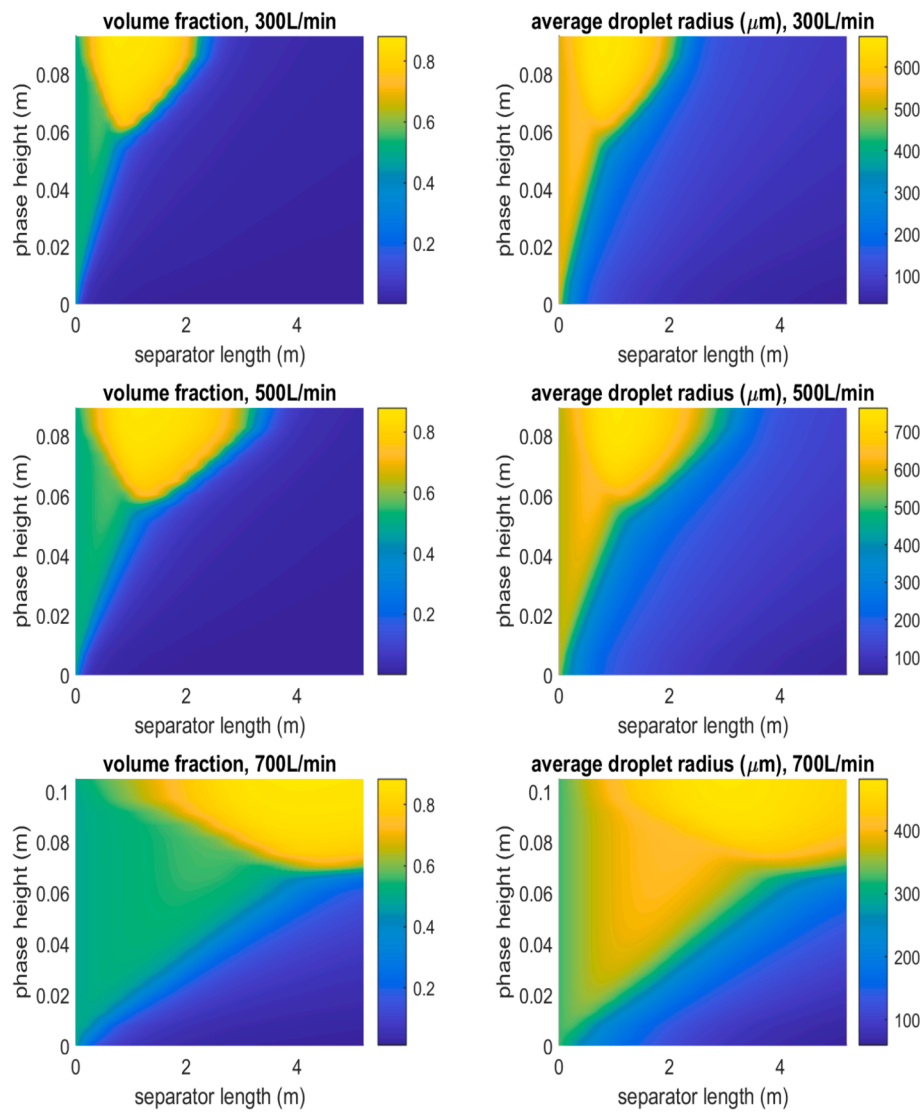


**Fig. 4.** Simulation results for dispersed phase volume fraction (left) and average droplet size (right) for WC = 50 % and varying volumetric flow rates (300, 500, 700 L/min from top to bottom).

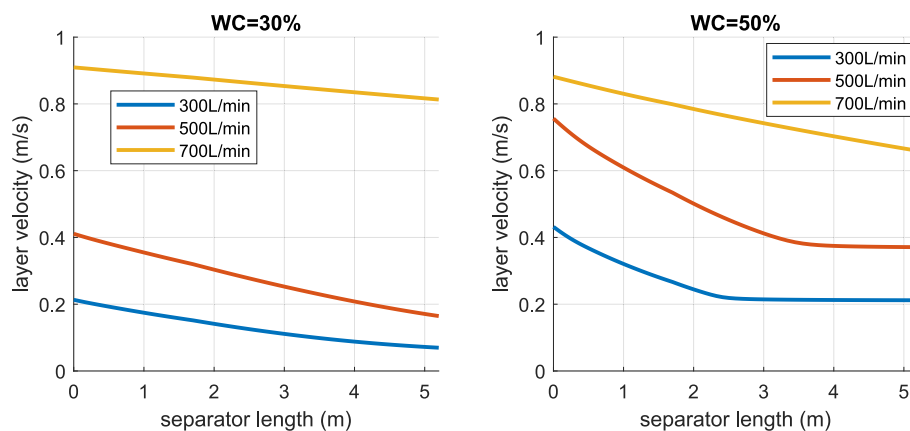


**Fig. 5.** Model prediction for velocity profiles along the separator length at different water-cuts and varying volumetric flow rates.

In Figs. 3 and 4, the horizontal axis is the length of the separator starting from the inlet of the sloped section and continuing to the end of the horizontal section, where the sloped section corresponds to 0–1.7 m.

In Fig. 3, the dispersed phase (i.e., oil) volume fraction is 70 %, whereas in Fig. 4, similar volumetric flows are simulated, but with a lower volume fraction of approximately 50 % for the dispersed phase.

According to the model assumptions stated in Section 5, the bottom layer is an oil-in-water dispersion, and the top layer is pure oil. This



means there is only transfer of oil droplets from the bottom dispersion layer to the top pure-oil layer. As a result of this droplet transfer, there is a decline in the total volume of oil in the bottom layer over the length of the separator, as depicted in the volume fraction contours in Figs. 3 and 4. This volume transfer from the bottom dispersion to the top pure-oil layer results in a decrease in the velocity of the bottom layer and an increase in the velocity of the top layer, as shown in Fig. 5.

In the initial set of simulations with a higher dispersed phase volume fraction (Fig. 3), it becomes apparent that the separation process is more challenging and less efficient. This can be attributed to the higher hindrance effect caused by the increased volume fraction in these cases. Conversely, in Fig. 4, the dispersed phase layer forms more rapidly, leading to a more efficient separation at the interface.

Furthermore, in the simulated scenarios depicted in Figs. 3 and 4, the total volumetric flow rate exhibits an ascending trend from 300 to 700 L/min. The impact of this variation in volumetric flow rate on the separation of phases becomes evident. As the flow rate increases, there is a noticeable reduction in residence time, thereby affecting the overall separation efficiency. Consequently, effective separation is attainable at lower liquid rates, but challenges arise at higher rates, necessitating the extension of the separator length in cases involving 700 L/min.

The velocity profiles predicted by the model along the length of the separator are provided in Fig. 5.

In Fig. 5, the velocity of the layer decreases along the length of the pipe separator. This phenomenon is attributed to the separation of the oil phase within this layer, subsequently being transferred to the upper layer at the interface.

In simulation cases with a water cut of 50 % and lower total volumetric flows (i.e., 300 and 500 L/min), the velocity experiences a more rapid decrease. Subsequently, the velocity profile curve becomes notably flat between the lengths of 2 and 4 m. This flattening is indicative of the complete depletion of the layer from the dispersed phase. However, for the case with a volumetric flow of 700 L/min, this point is not reached, highlighting the inadequacy of the separator length for this scenario. On the contrary, in simulation cases with a water cut of 30 %, attributed to a higher oil volumetric fraction, the layer velocity curves exhibit less pronounced slopes, and no flattening is achieved in any of the cases.

Notably, the apparent nonlinearity of velocity with respect to flow rate in Fig. 5 is due to the variations in the liquid levels across the three cases while the velocity still adheres to the Eq. (29).

The comparison of the model prediction and the experimental data

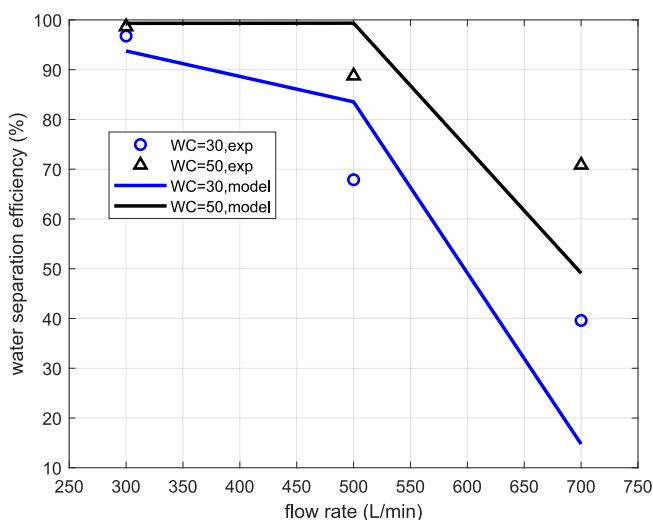


Fig. 6. Comparison of the experimentally measured water separation efficiency with predictions from the model for varying water-cuts and volumetric flow rates.

for the water separation efficiency is provided in Fig. 6.

Fig. 6 depicts two water-cuts, each consisting of three distinct operating conditions, with flow rates of 300, 500, and 700 L/min. As the volumetric flow increases, the separation efficiency declines as expected due to decreased residence time.

In the studied experiments, each case has slightly different conditions from others, including droplet size distribution and liquid level (details in the Supplementary material). Consequently, the conducted simulations are specific to these three operating points only, resulting in a non-smooth curve.

The model predictions follow the trend in the experimental data, but there are still differences due to the simplifications made in the model. Particularly, it can be attributed to the fact that we have set all the tuning parameters to unity. However, further work can be done to refine these models by adjusting the tuning parameters, which would require more data to provide reliable estimations.

## 6. Conclusion

A comprehensive model was formulated for 3-phase separators, divided into two primary sections: the inlet segment and the separation segment. The inlet section model incorporates a spatially homogeneous population balance model that accommodates turbulent droplet breakage and coalescence. The calculation of the turbulent energy dissipation rate involved an averaging strategy, considering the dynamic head of the multiphase stream in the inlet pipe.

The separation section model encompasses hydrodynamic models and dispersion models. The hydrodynamic models address the transported fluid volume between dispersion layers and consequent change in the velocity profiles, while the dispersion models account for turbulent-induced breakage and coalescence, as well as buoyancy-induced coalescence. This adaptability allows the model to be applied under normal operational conditions and during transient processes, such as start-up and shut-down scenarios.

In this investigation, a mathematical expression for the interfacial coalescence time of droplets was also developed. This expression is derived from the difference between gravitational and buoyant forces within a dense pack layer, establishing a connection between the thickness of the dense pack layer (DPL) and the rate of interfacial coalescence.

Furthermore, transient level dynamics have been integrated into the model, enabling the exploration of control schemes and transient upset conditions. To facilitate this, two separate solvers have been developed to handle both steady-state and transient problems.

To validate the mathematical model, predictions were compared against experimental data obtained from a multi-pipe separator, demonstrating good agreement.

There is potential for this work to be continued. In the future, we will focus on the following items:

- Validating cases with two dispersion layers in contact with mutual droplet transfer.
- Further tuning the model using more experimental data and exploring wider operating windows.

### Nomenclature

Symbol	definition	unit
$A$	cross section area of dispersion layer	$m^2$
$B$	Hamaker constant	$Nm^2$
$C_0$	model parameter for effective diffusion coefficient	$m$
$C_1, C_2, C_3, C_4$	coefficients in laminar velocity profiles	$m$
$D_e$	effective diffusion coefficient	$m^2s^{-1}$
$d_h$	hydraulic diameter	$m$
$ER$	extraction ratio	
$f$	radius-based volume density Distribution	$m^{-1}$
$F$	squeezing force	$N$

(continued on next page)



## Nomenclature (continued)

$F_{drop}$	squeezing force by a single droplet buoyancy force	$N$
$F_{DPL}$	squeezing force by DPL buoyancy force	$N$
$g$	gravitational acceleration	$ms^{-2}$
$H$	dispersion layer height	$m$
$K_B$	Boltzmann constant	$JK^{-1}$
$k_{b1}, k_{b2}$	empirical tuning parameters used in breakage model	
$k_{c1}, k_{c2}, k_{c3}, k_{c4}, k_{c5}$	empirical tuning parameters used in coalescence models	
$L_e$	effective length of the separation section	$m$
$l$	liquid level from bottom of the vessel	$m$
$\dot{m}$	mass flow rate	$kg s^{-1}$
$n_{ic}$	interfacial convective flux	$s^{-1}$
$P$	wetted perimeter	$m$
$Pe_{bc}$	droplet pair Peclet number used for binary coalescence	
$P_{DPL}$	squeezing pressure by DPL buoyancy force	$Pa$
$Q$	volumetric flow rate	$m^3 s^{-1}$
$R$	cylindrical vessel radius	$m$
$R_{bb}$	breakage birth rate for radius-based volume density	$m^{-1} s^{-1}$
$R_{bd}$	breakage death rate for radius-based volume density	$m^{-1} s^{-1}$
$R_{cb}$	coalescence birth rate for radius-based volume density	$m^{-1} s^{-1}$
$R_{cd}$	coalescence death rate for radius-based volume density	$m^{-1} s^{-1}$
$Re$	Reynolds number	
$r$	droplet radius	$m$
$SE$	separation efficiency	
$T$	absolute temperature	$K$
$t$	time	$s$
$t_{bc}$	binary film drainage and rupture (coalescence) time	$s$
$t_{ic}$	interfacial film drainage and rupture (coalescence) time	$s$
$t_f$	final time	$s$
$t_r$	residence time	$s$
$u$	velocity	$ms^{-1}$
$u_{ic}$	equivalent droplet interfacial velocity for a coalescing droplet	$ms^{-1}$
$u_s$	slip velocity between continuous and dispersed phases	$ms^{-1}$
$V$	volume	$m^3$
$w$	width of dispersion layer formed as a circular segment	$m$
$W$	width of dispersion layer when geometrically mapped to a rectangle	$m$
$y$	vertical direction variable	$m$
$z$	axial direction variable	$m$
<b>Greek symbol</b>	<b>definition</b>	<b>unit</b>
$\alpha$	water cut in the inlet stream	
$\beta$	radius-based daughter distribution	$m^{-1}$
$\gamma$	breakage frequency	$s^{-1}$
$\delta$	angle between the separator's axial direction and the horizontal axis	
$\varepsilon$	turbulent energy dissipation rate	$m^2 s^{-3}$
$\theta$	central angle for a circular segment	$rad$
$\kappa$	coalescence rate	$m^3 s^{-1}$
$\mu$	dynamic viscosity	$Nm^{-2} s$
$\mu_r$	average droplet radius	$m$
$\nu$	kinematic viscosity	$m^2 s^{-1}$
$\rho$	density	$kg m^{-3}$
$\sigma$	interfacial tension	$Nm^{-1}$
$\varphi$	split factor	
$\phi$	volume fraction	
$\phi_m$	model parameter for effective diffusion coefficient	
$\psi$	binary droplet coalescence efficiency	
$\omega$	binary droplet collision rate	$m^3 s^{-1}$
<b>Subscript</b>	<b>definition</b>	
$0$	initial condition	
$b$	buoyancy-induced coalescence	
$c$	continuous phase	
$d$	dispersed phase	
$DPL$	dense packed layer	
$i$	dispersion layer identifier (oc or wc)	
$in$	inlet	
$IS$	inlet section	
$l$	liquid mixture	
$o$	oil phase	
$oc$	oil-continuous dispersion layer	

(continued on next column)

## Nomenclature (continued)

$oi$	oil inlet stream
$out$	outlet
$SS$	separation section
$t$	turbulent-induced coalescence/breakage
$w$	water phase
$wc$	water-continuous dispersion layer
$wi$	water inlet stream
$wo$	water outlet stream

## CRediT authorship contribution statement

**Moein Assar:** Writing – original draft, Visualization, Software, Methodology, Investigation, Formal analysis, Conceptualization. **Hamidreza Asaadian:** Investigation, Data curation. **Milan Stanko:** Writing – review & editing, Project administration. **Brian Arthur Grimes:** Writing – review & editing, Supervision, Project administration, Conceptualization.

## Declaration of competing interest

The authors declare the following financial interests/personal relationships which may be considered as potential competing interests: Moein Assar reports financial support was provided by The Research Council of Norway. If there are other authors, they declare that they have no known competing financial interests or personal relationships that could have appeared to influence the work reported in this paper.

## Data availability

Data will be made available on request.

## Acknowledgments

This work was carried out as a part of SUBPRO, a Research-Based Innovation Centre within Subsea Production and Processing. The authors gratefully acknowledge the financial support from SUBPRO, which is financed by the Research Council of Norway, major industry partners, and NTNU.

## Appendix A. Supplementary data

Supplementary data to this article can be found online at <https://doi.org/10.1016/j.ces.2024.120375>.

## References

- Antonio García, A., Berres, S., Mas-Hernández, E., 2022. A new mathematical model of continuous gravitational separation with coalescence of liquid-liquid emulsions. *Chem. Eng. Res. Des.* 182, 37–50. <https://doi.org/10.1016/J.CHERD.2022.03.044>.
- Antonio García, A., Fernando Betancourt, C., 2019. Conservative mathematical model and numerical simulation of batch gravity settling with coalescence of liquid-liquid dispersions. *Chem. Eng. Sci.* 207, 1214–1229. <https://doi.org/10.1016/j.ces.2019.07.034>.
- Asaadian, H., Stanko, M., 2023. Experimental characterization and evaluation of crude spiking influence on oil/water dispersed flow in pipe. *Molecules* 28, 6363 <https://doi.org/10.3390/MOLECULES28176363>.
- Asaadian, H., Harstad, S., Stanko, M., 2022. Drainage potential curves of single tapping point for bulk oil-water separation in pipe. *Energies* 15, 6911. <https://doi.org/10.3390/EN15196911>.
- Asaadian, H., Stanko, M., 2023. Experimental quantification of the performance of a horizontal multi-pipe bulk separator of water and oil with crude spiking. *J. Pet. Explor. Prod. Technol.* 13, 2283–2302. <https://doi.org/10.1007/S13202-023-01672-9>.
- Assar, M., Grimes, B.A., 2022. A new approach to analyze the equilibrium and transient behaviors of particulate systems and the subsequent application to multiphase fluid systems. *Chem. Eng. Res. Des.* 188, 1083–1096. <https://doi.org/10.1016/J.CHERD.2022.10.044>.
- Assar, M., Simon, S., Sørland, G.H., Grimes, B.A., 2023. A theoretical and experimental investigation of batch oil-water gravity separation. *Chem. Eng. Res. Des.* 194, 136–150. <https://doi.org/10.1016/J.CHERD.2023.04.029>.

- Backi, C.J., Grimes, B.A., Skogestad, S., 2018. A control- and estimation-oriented gravity separator model for oil and gas applications based upon first-principles. *Ind. Eng. Chem. Res.* 57, 7201–7217. <https://doi.org/10.1021/ACS.IECR.7B04297>.
- Behzadi, A., Issa, R.I., Rusche, H., 2004. Modelling of dispersed bubble and droplet tow at high phase fractions. *Chem. Eng. Sci.* 59, 759–770. <https://doi.org/10.1016/j.ces.2003.11.018>.
- Bin Ismail, A.S., 2021. Modeling the Dynamic Evolution of Drop Size Density Distribution of the Oil-Water Emulsion in Turbulent Pipe Flow. NTNU.
- Bird, R.B., Stewart, W.E., Lightfoot, E.N., 2006. *Transport Phenomena, Revised, 2nd Edition*. John Wiley & Sons Ltd.
- Bothamley, M., 2013. Gas/liquid separators: quantifying separation performance - Part 1. *Oil Gas Facil.* 2, 21–29. <https://doi.org/10.2118/0813-0021-OGF>.
- Chesters, A.A., 1991. The modelling of coalescence processes in fluid-liquid dispersions: A review of current understanding. *Chem. Eng. Res. Des.* 69, 259–270.
- Coulaloglou, C.A., Tavarides, L.L., 1977. Description of interaction processes in agitated liquid-liquid dispersions. *Chem. Eng. Sci.* 32, 1289–1297. [https://doi.org/10.1016/0009-2509\(77\)85023-9](https://doi.org/10.1016/0009-2509(77)85023-9).
- Cunha, R.E.P., Fortuny, M., Dariva, C., Santos, A.F., 2008. Mathematical modeling of the destabilization of crude oil emulsions using population balance equation. *Ind. Eng. Chem. Res.* 47, 7094–7103. <https://doi.org/10.1021/IE800391V>.
- Dale Anderson, V.S., Tannehill, J.C., Pletcher, R.H., Munipalli, R., 2020. *Computational Fluid Mechanics and Heat Transfer*. CRC Press.
- Gear, C.W., 1971. *Numerical Initial Value Problems in Ordinary Differential Equations, 1st ed.* Prentice Hall.
- Grimes, B.A., 2012. Population balance model for batch gravity separation of crude oil and water emulsions. Part I: Model formulation. *J. Dispers. Sci. Technol.* 33, 578–590. <https://doi.org/10.1080/01932691.2011.574946>.
- Grimes, B.A., Dorao, C.A., Opedal, N.V.D.T., Kralova, I., Sørland, G.H., Sjöblom, J., 2012. Separation data. *J. Dispers. Sci. Technol.* 33, 591–598. <https://doi.org/10.1080/01932691.2011.574950>.
- Hahn, P.-S., Slattery, J.C., 1985. Effects of surface viscosities on the stability of a draining plane parallel liquid film as a small bubble approaches a liquid-gas interface. *AIChE J.* 31, 950–956. <https://doi.org/10.1002/AIC.690310611>.
- Kumar, A., Hartland, S., 1985. Gravity settling in liquid/liquid dispersions. *Can. J. Chem. Eng.* 63, 368–376. <https://doi.org/10.1002/CJCE.5450630303>.
- Liao, Y., Rzehak, R., Lucas, D., Krepper, E., 2015. Baseline closure model for dispersed bubbly flow: Bubble coalescence and breakup. *Chem. Eng. Sci.* 122, 336–349.
- Oshinowo, L.M., Vilagines, R.D., 2020. Modeling of oil–water separation efficiency in three-phase separators: Effect of emulsion rheology and droplet size distribution. *Chem. Eng. Res. Des.* 159, 278–290. <https://doi.org/10.1016/j.CHERD.2020.02.022>.
- Oshinowo, L.M., Quintero, C.G., Vilagines, R.D., 2016. CFD and population balance modeling of crude oil emulsions in batch gravity separation—Comparison to ultrasound experiments. *J. Dispers. Sci. Technol.* 37, 665–675. <https://doi.org/10.1080/01932691.2015.1054508>.
- Pal, R., Rhodes, E., 1989. Viscosity/concentration relationships for emulsions. *J. Rheol.* (N. Y. N. Y.) 33, 1021–1045. <https://doi.org/10.1122/1.550044>.
- Panjwani, B., Amiri, A., Mo, S., Fossen, M., Linga, H., Pauchard, V., 2015. Dense packed layer modeling in oil-water dispersions: model description, experimental verification, and code demonstration. *J. Dispers. Sci. Technol.* 36, 1532–2351. <https://doi.org/10.1080/01932691.2014.1003221>.
- Prince, M.J., Blanch, H.W., 1990. Bubble coalescence and break-up in air-sparged bubble columns. *AIChE J.* 36, 1485–1499. <https://doi.org/10.1002/aic.690361004>.
- Richardson, J.F., Zaki, W.N., 1954. The sedimentation of a suspension of uniform spheres under conditions of viscous flow. *Chem. Eng. Sci.* 3, 65–73. [https://doi.org/10.1016/0009-2509\(54\)85015-9](https://doi.org/10.1016/0009-2509(54)85015-9).
- Rogers, J.R., Davis, R.H., 1990. Modeling of collision and coalescence of droplets during microgravity processing of Zn-Bi immiscible alloys. *Metall. Trans.* 21, 59–68. <https://doi.org/10.1007/BF02656424>.
- Ruiz, M.C., Padilla, R., 1996. Separation of liquid-liquid dispersions in a deep-layer gravity settler: Part II. Mathematical modeling of the settler. *Hydrometallurgy* 42, 281–291. [https://doi.org/10.1016/0304-386X\(95\)00096-Y](https://doi.org/10.1016/0304-386X(95)00096-Y).
- Schümann, H., 2016. Experimental Investigation of Transitional Oil-Water Pipe Flow. NTNU <http://hdl.handle.net/11250/2396843>.
- Skjefstad, H.S., Stanko, M., 2018. An experimental study of a novel parallel pipe separator design for subsea oil-water bulk separation. In: *Soc. Pet. Eng. - SPE Asia Pacific Oil Gas Conf. Exhib.* 2018. APOGCE. <https://doi.org/10.2118/191898-MS>.
- Skjefstad, H.S., Stanko, M., 2019. Experimental performance evaluation and design optimization of a horizontal multi-pipe separator for subsea oil-water bulk separation. *J. Pet. Sci. Eng.* 176, 203–219. <https://doi.org/10.1016/J.PETROL.2019.01.027>.
- Skjefstad, H.S., Dudek, M., Øye, G., Stanko, M., 2020. The effect of upstream inlet choking and surfactant addition on the performance of a novel parallel pipe oil–water separator. *J. Pet. Sci. Eng.* 189, 106971. <https://doi.org/10.1016/J.PETROL.2020.106971>.
- Vankova, N., Tcholakova, S., Denkov, N.D., Vulchev, V.D., Danner, T., 2007. Emulsification in turbulent flow. 2. Breakage rate constants. *J. Colloid Interface Sci.* 313, 612–629. <https://doi.org/10.1016/J.JCIS.2007.04.064>.
- Villadsen, J., Michelsen, M.L., 1978. *Solution of Differential Equation Models by Polynomial Approximation*. Prentice-Hall, Englewood Cliffs, New York.
- Wang, H., Davis, R.H., 1995. Simultaneous sedimentation and coalescence of a dilute dispersion of small drops. *J. Fluid Mech.* 295, 247–261. <https://doi.org/10.1017/S0022112095001959>.